Pressure-dependent modifications in the $LaAuSb_2$ charge density wave system

Govindaraj Lingannan,[1] Boby Joseph,[2,*] Ponniah Vajeeston,[3] Chia Nung Kuo,[4] Chin Shan Lue,[4] Ganesan Kalaiselvan,[1] Piu Rajak,[5,6] and Sonachalam Arumugam[1,†]

[1]*Center for High Pressure Research (CHPR), School of Physics, Bharathidasan University, Tiruchirappalli 620024, India*

[2]*Elettra-Sincrotrone Trieste S.C. p. A., S.S. 14, Km 163.5 in Area Science Park, Basovizza 34149, Italy*

[3]*Department of Chemistry, Centre for Materials Science and Nanotechnology, University of Oslo, P.O. Box 11126, Blindern, N-0318 Oslo, Norway*

[4]*Department of Physics, National Cheng Kung University, Tainan 70101, Taiwan*

[5]*CNR-IOM TASC National Laboratory, Area in Science Park- Basovizza, 34149, Trieste, Italy*

[6]*Abdus Salam International Centre for Theoretical Physics, Via Beirut, 6, 34151, Trieste, Italy*

(Received 2 January 2021; revised 21 April 2021; accepted 27 April 2021; published 12 May 2021)

Hydrostatic pressure response of $LaAuSb_2$ charge density wave (CDW) system is investigated using electrical transport, x-ray diffraction (XRD), and density-functional theory (DFT). Resistivity data at ambient pressure evidence a clear CDW transition at 83 K. X-ray diffraction at ambient pressure reveals that in plane and out of plane axes show opposite behavior with decreasing temperature, in particular, out of plane c axis develops a distinct change at ∼250 K, much above the observed CDW transition at 83 K. The CDW transition shifts to low temperature with increasing pressure. Our resistivity data indicate a complete suppression of the CDW transition at ∼3.6 GPa. High-pressure XRD revealed a change from the linear trend for the out of plane (c) and the in plane (a) lattice parameters for pressure above 3.8 GPa. With compression, DFT indicated an anomaly in the c/a ratio around 8 GPa. The calculated electronic structure also indicated minor changes in the band structure in this pressure range. In addition, high-pressure DFT structural investigations reveal the $LaAuSb_2$ system to be stable up to pressures as high as 150 GPa.

DOI: 10.1103/PhysRevB.103.195126

I. INTRODUCTION

A charge density wave (CDW) is a phenomenon in solids driven by the Fermi surface (FS) due to a static modulation of conduction charge carriers which is usually followed by a periodic lattice distortion. Distortion decreases the electronic energy of the solid and energy of the corresponding strain is more than compensated by the reduction in electronic energy [1]. Peierls (1955) suggested that a simple one-dimensional solid is vulnerable to a periodic distortion of the lattice that can minimize the overall energy [2]. The term CDW was first used by Fröhlich [3]. A detailed explanation of CDW was provided by Wilson *et al.* in 1975 using the $4d^1/5d^1$ dichalcogenides [4]. Zhu *et al.* classified the CDW into three categories; the first category is quasi-1D systems where the origin of CDW is Fermi-surface nesting (FSN). The second category is regulated by electron-phonon coupling (EPC) and $NbSe_2$ systems fall in this category. The third category is a charge modulation or charge ordering (CO)-based one with no indication of FSN or EPC. Classical high-temperature superconducting cuprates exhibit CO [5]. The CDW phenomenon [6–11], particularly its coexistence and interplay of CDW and superconductivity, is an important field of study in recent years [12–17]. In several systems, it is found that external pressure [18–20] or chemical doping [21,22] can suppress the CDW transition and induce superconductivity. The CDW phenomenon is also observed in some of the ternary antimonides: $LnTMSb_2$ (Ln = rare earth, TM = transition metal) such as $LaAgSb_2$ [23,24] and $LaAuSb_2$ [25,26]. Ternary antimonides crystallize in tetragonal $ZrCuSi_2$-type structure ($P4/nmm$) [23,27–29] where planar two-dimensional layers of Sb, TM, and Ln-Sb are stacked along the c axis. This structural configuration has a close similarity with the iron-pnictide superconductors [30]. Apart from CDW, $LnTMSb_2$ systems show various phenomena such as superconductivity ($LaNiSb_2$, $LaCuSb_2$, and $LaPdSb_2$ [31]), quantum critical point ($CeAuSb_2$ [32]), and ferromagnetism ($CeAgSb_2$ [33]), where the Ln $4f$ electron number, TM element and the crystal structural parameters are found to play an important role.

In $LaAgSb_2$, Song *et al.* [34] observed two CDW transitions at ∼207 K (T_{CDW1}) and 185 K (T_{CDW2}) perpendicular and parallel to the c direction, respectively. $LaAuSb_2$ is isostructural to $LaAgSb_2$, and it exhibits a similar CDW transition at ∼88 K as evidenced from the resistivity data [23]. The CDW phase transition is understood as due to a partial gapping of the FS's through electrical transport, thermoelectric, and ultrafast pump-probe spectroscopy measurements [25]. In $LaAu_xSb_2$, Xiang *et al.* [26] recently observed two CDW transitions at ∼110 and ∼90 K by careful electrical transport measurements. Further, they could tune the CDW transition in $LaAu_xSb_2$ via chemical and physical

*boby.joseph@elettra.eu
†sarumugam1963@yahoo.com

pressure [26]. The CDW temperature decreases monotonically while decreasing the x value from $T_{CDW1} = 110$ K ($x = 0.991$) to $T_{CDW1} = 33$ K ($x = 0.913$) and it reduces the unit-cell volume. The application of pressure of ~0.75 and ~1.7 GPa leads to suppression of lower transition and upper transition, respectively [26]. Study of Xiang *et al.*, did not indicate any observation of superconductivity in the $LaAu_xSb_2$; however, it should be noted that the minimum temperature they reached was 1.8 K. In contrast, a recent study by Du *et al.* [35], showed superconductivity in $LaAuSb_2$ at an extremely low temperature of ~0.6 K with a CDW transition around 78 K. Pressure of about 0.64 GPa is found to suppress the CDW transition completely which concurrently leads to an enhancement in the superconducting transition temperature to 1.05 K. Here, we investigate synchrotron x-ray powder-diffraction study as a function of temperature (from 390 to 110 K) and pressure (from 0 to 8.86 GPa) for $LaAuSb_2$ with very similar CDW properties. However, the CDW transition that we observe is about 83 K. Further, resistivity measurements as a function of temperature (300 to 4 K) under various hydrostatic pressures (0 to 3.14 GPa) and DFT calculations are performed to understand the correlation between structural and transport properties. Our results, together with earlier studies on this system, will contribute to the understanding of the CDW phenomena in the ternary antimonide $LaAuSb_2$.

II. METHODS

A. Experimental methods

$LaAuSb_2$ single crystals were prepared by the self-flux method using mixtures of La (99.9%), Au (99.9%), and Sb (99.9%) in the ratio of 1:2:20. Detailed synthesis procedures were described in Ref. [25]. The synthesized sample was found to be not air sensitive.

Scanning electron microscopy (SEM) and energy-dispersive x-ray spectroscopy (EDX) data were carried out by a ZEISS Supra 40 field-emission gun equipped with an EDX system. SEM was equipped with a Gemini column and an in-lens detector yielding increased signal-to-noise ratio. The relative composition of the sample is determined by collecting backscattered electrons, which is proportional to the average atomic number. The quantitative composition is determined from EDX spectrum image maps measured in SEM. The spectrum image maps were constructed by collecting the full EDX spectrum at each pixel. Figure 1 shows SEM backscattered electron image together with EDX elemental maps of antimony, lanthanum, and gold. A typical EDX spectrum is shown in Supplemental Material, Fig. S1 [36]. Elemental maps show that all three elements have very similar spatial distribution. The quantitative information on the chemical composition shows an almost equal amount of La and Au and two times antimony, respectively, 25.7, 24.13, and 50.17.

Temperature-dependent x-ray powder-diffraction (XRPD) data were collected at the XRD1 beamline of the Elettra-Synchrotron Center, Trieste, Italy using a cryojet (model Oxford700) with small temperature steps using a wavelength of 0.7 Å. The experimental setup for XRPD and the data collection procedure were similar to those described in Ref. [37].

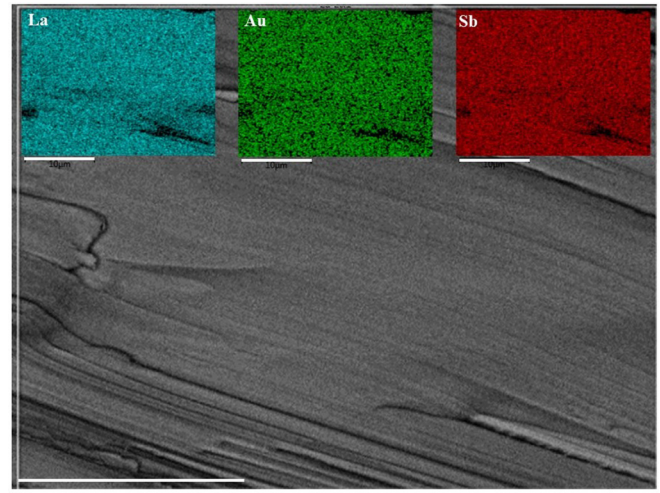

FIG. 1. SEM image reconstructed from the backscattered electrons (main frame) together with the EDX elemental maps. The scale bar in all cases indicates 10 μm. The atomic percentage obtained from the EDX analysis are Sb: 50.17, Au: 24.13, and La: 25.7.

The electrical resistivity was measured on bar-shaped sample by a standard linear four-probe DC resistivity technique in a cryogen-free closed-cycle refrigerator (CCR-VTI) in the temperature range of 4–300 K. Silver paste (4929N) and copper wire (Φ 0.05 mm) were used to make the electrical contacts on the sample. Hydrostatic high-pressure electrical resistivity measurements have been carried out using clamp-type hybrid double-cylinder (NiCrAl-inner cylinder; BeCu-outer cylinder) piston pressure cell. The pressure-transmitting medium (Daphne oil 7474) was used and previously obtained fixed-pressure points of bismuth calibration were used to estimate actual pressure inside the pressure cell [38].

High-pressure x-ray-diffraction studies were carried out at the Xpress beamline [39] of Elettra. Two pressure runs were performed. A gear-driven Bohler-Almax plate diamond-anvil cell (DAC) was used for the x-ray high-pressure diffraction for the first. In this case, silicone oil was used as the pressure-transmitting medium (PTM). For the high-pressure diffraction data collection, a MAR345 image plate is used. For the second run, a membrane-driven symmetric DAC was used together with a PACE5000-based automatic membrane drive. PTM used in this case was 4:1 methanol-ethanol mixture. In both runs, the pressure was monitored *in situ* by ruby fluorescence method, by including a ruby chip (~10 μm) along with the sample in the pressure cell. In both cases, high-pressure diffraction data collection was performed by a monochromatic circular beam with a wavelength of 0.495 Å and a beam cross-sectional diameter ~40 μm. For the second run, a Pilatus3S-6M large-area detector was used for the diffraction data collection. This detector has isolated active pixels together with the possibility to be at a further distance to cover the same angular range for diffraction. These favorably contributed to a slightly better resolution in the second run compared to first. All the data related to the first run are shown in the Supplemental Material [36]. Images of the powder-diffraction rings from the MAR345 and Pilatus3S 6M were converted into 2θ intensity plots by the FIT2D software.

FULLPROF suite was used to refine the structural model using the Rietveld method.

B. Computational methods

Total energies have been calculated by the projected-augmented plane-wave implementation of the Vienna *Ab initio* Simulation Package (VASP) [40,41]. All these calculations were made using the Perdew-Burke-Ernzerhof [42] exchange-correlation functional. Ground-state geometries were determined by minimizing both the stresses and the Hellman-Feynman forces using the conjugate-gradient algorithm with a force convergence threshold of 10^{-3} eV Å^{-1}. Brillouin-zone integration was performed with a Gaussian broadening of 0.1 eV during all relaxations. From various sets of calculations, it was found that 2050 **k** points in the Brillouin zone for the structure with a 600-eV plane-wave cutoff are sufficient to ensure optimum accuracy in the computed results. The **k**-points mesh was generated using the Monkhorst-Pack method with a grid size of 10 × 10 × 4 for structural optimization. Iterative relaxation of atomic positions was stopped when the change in total energy between successive steps was smaller than 1 meV/cell.

A frozen phonon calculation was performed on the supercells using the PHONOPY program to obtain the phonon dispersion curve and density of states [43]. An atomic displacement of 0.0075 Å was used, with a symmetry consideration, to obtain the force constants for the phonon calculations. The displacements in opposite directions along all axes were incorporated in the calculations to improve the overall precision. The force calculations were made using the VASP code with the supercell approach and the resulting data were imported into the PHONOPY program. The dynamical matrices were calculated from the force constants, and phonon density of states (DOS) curves were computed using the Monkhorst-Pack scheme [44]. The thermal properties, such as heat capacity, free energy, and entropy, were obtained using the calculated phonon DOS.

The calculated total energy as a function of volume has been fitted to the universal equation of state (EoS) [45]. The transition pressures are calculated from the pressure versus Gibbs free-energy curves. The Gibbs free energy ($G = U + PV - TS$, where $T = 0$; G = total energy + pressure × volume) is calculated in the following way: the volume versus total energy curve is fitted to the universal EoS function. The pressure is defined as $P = (B_0/B_0^{|}) \times [(v_e/v^{B0'} - 1]$. The relation can be inverted to obtain the volume as $(v) = v_e/[(1 + (B_0^{|}/B_0 \times p)^{1/B0'}]$, where v_e, B_0, and $B_0^{|}$ refer to the equilibrium volume, the bulk modulus, and its derivative with respect to pressure, respectively. The inverse is then calculated using the bisection method. From the scan over the pressures, the corresponding difference in the enthalpy between the two datasets was calculated.

III. RESULTS AND DISCUSSION

A. Ambient pressure results

Figure 2 shows the powder x-ray-diffraction pattern of $LaAuSb_2$ sample at ambient pressure and temperature at 400 K. The XRPD results show that the synthesized sample has a tetragonal $ZrCuSi_2$-type structure with space group *P4/nmm* and lattice parameters $a = 4.441$ Å and $c = 10.435$ Å at room temperature. Single-crystal diffraction [Fig. S1(a)] from inside the DAC confirmed the space-group and atomic positions at ambient conditions to be similar to that given in Ref. [25]. We also observed 0.5% of Sb as an impurity in the studied sample (notice * symbols in Fig. 2). A schematic view of the tetragonal crystal structure of $LaAuSb_2$ is shown in Fig. 2. Antimony atoms occupy two nonequivalent crystallographic sites (Sb_1 and Sb_2) with the Sb_1 group forming a 2D sheet structure. The structure can be viewed as a stack of Au-$LaSb_2$-Sb_1-$LaSb_2$-Au layers along the *c* axis. In order to understand the dynamical stability of the $LaAuSb_2$, we carried out the phonon calculations. The calculated vibrational spectrum curves together with the corresponding site projected density of states are plotted in Figs. 3(a) and 3(b), respectively. The positive phonon frequencies suggest that $LaAuSb_2$ is dynamically stable. The vibrational modes are spread over from 0 to 5.2 THz. As expected, based on the relationship between masses and frequencies the heavier element Au is normally connected with the lower frequencies. The lattice vibrational modes for Au, La, and Sb are present in the 0.5 to 2.1-THz range, 2.43 to 4-THz range, and 0.4 to 5.2-THz range, respectively.

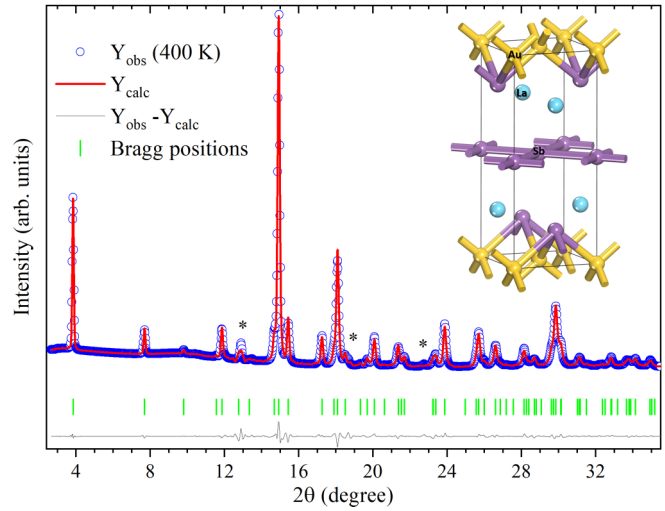

FIG. 2. Measured x-ray-diffraction pattern of $LaAuSb_2$ sample at ambient pressure and 400 K (symbols) together with the Rietveld refinement results (solid red lines). The 0.7-Å wavelength was used. Green vertical bars below the diffractogram indicate the Bragg peak positions and * indicates the Sb impurity peaks. Inset shows the tetragonal crystal structure of $LaAuSb_2$ where antimony occupies two distinct positions Sb1 (0.75, 0.25, 0.5) in between La layers and Sb2 (0.25, 0.25, 0.1706) close to Au.

The calculated electronic band structure is shown in Fig. 3(c). The total DOS together with the site projected partial DOS are shown in Fig. 3(d). Electronic DOS at Fermi level (E_F) is small but finite, underlining the $LaAuSb_2$ to be metallic. The bands distribution within the Brillouin zone is found to be highly anisotropic. For example, the bands' crossover between the valence and conduction band in the Γ-*X*, **M**-Γ, and *Z*-*R* direction is a nominal metallic feature, while, due to the layered nature of the crystal the bands at

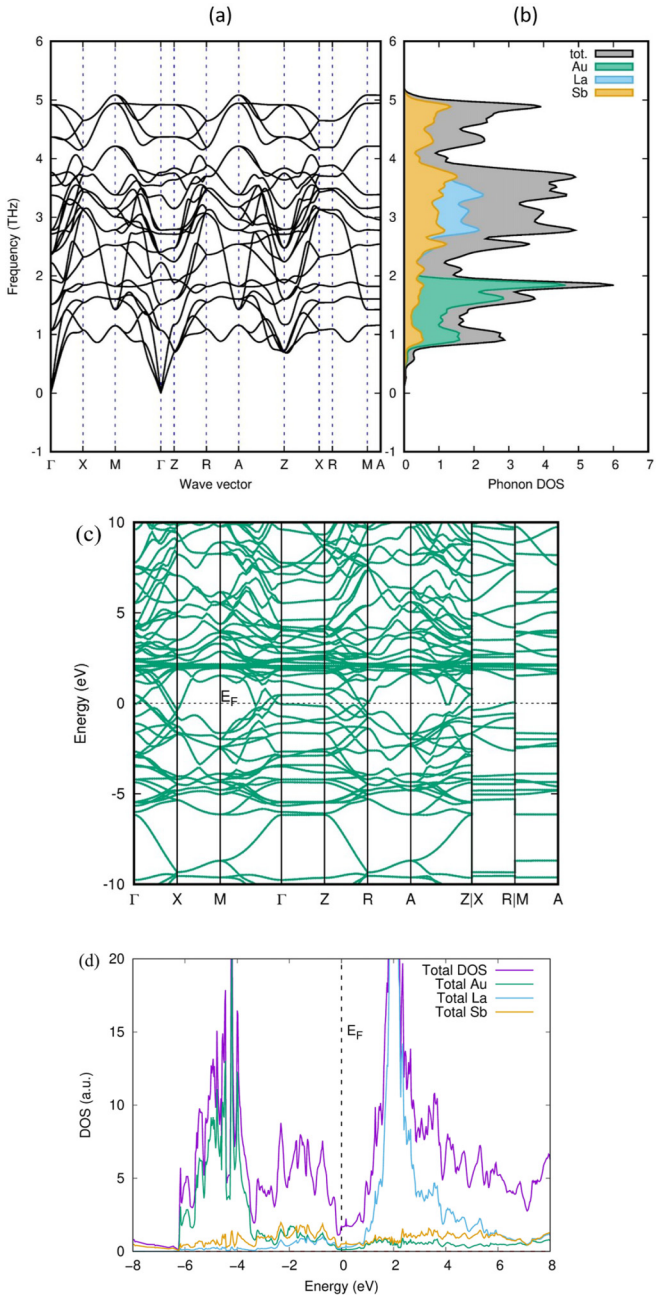

FIG. 3. Calculated phonon spectra (a), site-projected phonon density of states (b), electronic band structure (c), and total electronic DOS (d) for $LaAuSb_2$ at ambient pressure. General gradient approximation (GGA) and Perdew-Wang (PW91) functionals are used for the computation.

Γ-*Z*, *X*-*R*, and *M*-*A* directions are almost flat. Because of this reason, the DOS near the E_F is almost flat and up to 0.3 eV in the conduction band.

The theoretically obtained structural parameters and the positional parameters are presented along with experimental data in Table I. From this table, it is clear that the equilibrium structural parameters obtained from our theoretical calculations are in good agreement with the corresponding experimental findings. The calculated cell parameters are differing within 1.5% with the experimental values.

TABLE I. Experimental (300 K) and DFT structural parameters in $P4/nmm$ (number 129) space group.

	Experimental values	Theoretical values
a, *c* (Å)	4.441, 10.4351	4.4836, 10.4988
La (2*c*)	1/4, 1/4, 0.7454	1/4, 1/4, 0.7527
Au (2*a*)	3/4, 1/4, 0	3/4, 1/4, 0
Sb (2*b*)	3/4, 1/4, 0.5	3/4, 1/4, 0.5
Sb (2*c*)	1/4, 1/4, 0.1708	1/4, 1/4, 0.1731

The temperature dependence of electrical resistivity data from 4 to 300 K at six different pressures is shown in Fig. 5(a). From the ambient pressure data, one can notice a clear CDW anomaly at 83 K (inset shows the derivative which can used for a ready identification of the transition temperature). Figure 4(a) shows the temperature dependence of in plane *a*- and out of plane *c*-lattice parameters. Lattice parameter *a* increases with increasing temperature; however, *c* decreases with increasing temperature, and rate of shrinkage is increased above 250 K [green arrow in Fig. 4(a)]. Thus, there is a negative thermal expansion for the lattice parameter *c*. We discuss this aspect in the later part of the paper while describing the pressure-dependent structural data from DFT. However, the unit-cell volume shows no significant anomalies with temperature, revealing only a regular temperature-dependent contraction with decreasing temperature [Fig. 4(b)]. The out of plane to in plane ratio (c/a ratio) shows an increase from ∼2.342 at 400 K to ∼2.361 at 110 K [Fig. 4(c)], but with a changing trend around 250 K. From the earlier studies, it is noted that with decreasing temperature, a partial gapping developed at FS's related to the CDW transition [25] which is also correlated with a modulation of lattice captured in the current investigation. For obtaining the exact nature of the lattice modulation related to the CDW transition, further involved x-ray scattering techniques may be useful, similar to the one reported for $LaAgSb_2$ [34].

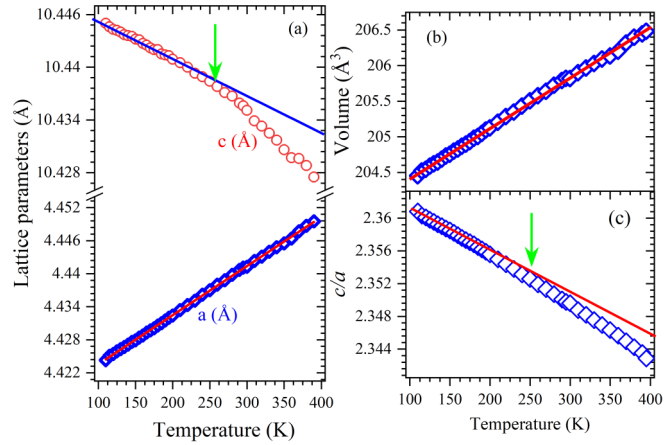

FIG. 4. Temperature dependence of the out of plane to in plane lattice parameters (a). Temperature dependence of the unit-cell volume (b) and c/a ratio (c). Green arrows in (b) and (c) indicate temperature at which a deviation from the expected linear trend (solid line) occurs.

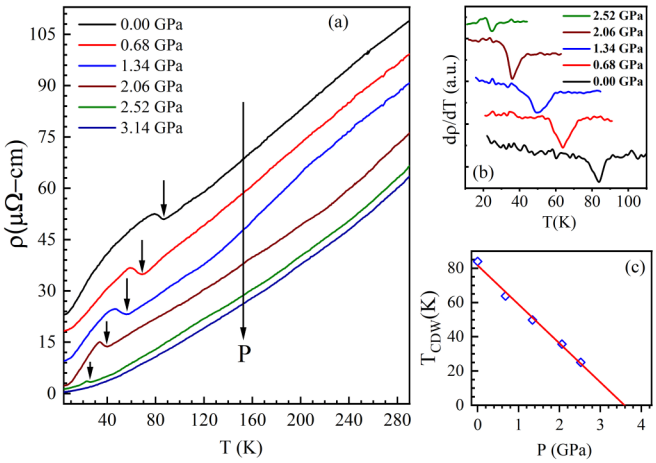

FIG. 5. (a) Temperature dependence of electrical resistivity measurements under various hydrostatic pressures. (b) First derivative of the temperature dependence of electrical resistivity demonstrating the CDW transition temperature and (c) T_{CDW} vs pressure.

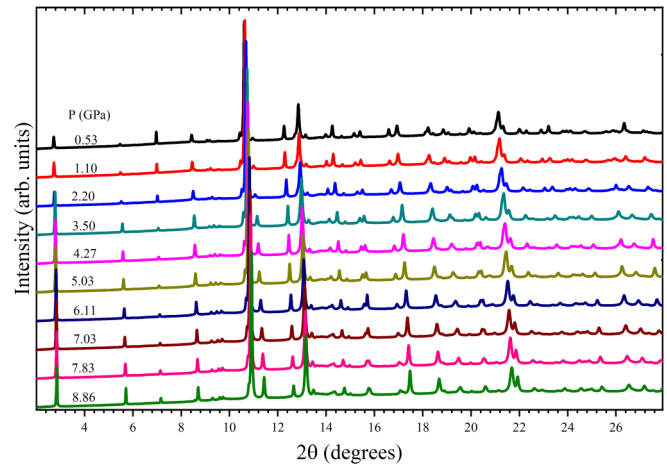

FIG. 6. Measured x-ray-diffraction pattern of $LaAuSb_2$ at several pressures up to 9 GPa using 4:1 methanol-ethanol as pressure-transmitting medium. Patterns are shifted vertically for clarity in presentation.

B. High-pressure resistivity

As noted before, Fig. 5 shows the temperature dependence of electrical resistivity measurements under various hydrostatic pressures up to 3.14 GPa. At ambient pressure resistivity measurement shows the CDW transition at ∼83 K. Opening of a partial gap at Fermi surface below 83 K [25] is the cause for the increase of resistivity. Figure 5(b) shows the temperature derivative of resistivity data of $LaAuSb_2$ with various fixed pressures. Data shown in Fig. 5(c) demonstrate that the pressure decreases the CDW transition monotonically. Our data at 3.14 GPa do not evidence a clear CDW transition. It is to be noted that in our measurements the minimum temperature reached was 4 K; thus, we are not able to detect possible CDW or superconducting transitions below 4 K. A linear extrapolation of obtained CDW temperatures to 0 K indicates the full suppression to occur at around 3.6 GPa [Fig. 5(c)]. We note that a recent study on a very similar system showed the full suppression of the CDW at much lower pressure about ∼0.64 GPa [35]. In $LaAu_xSb_2$ system, it was shown that the CDW transition can be tuned by changing gold concentration [26]. The difference that we observe from the earlier study reveals the complexity of apparently simple ternary antimonide systems.

C. Structural response to CDW at high pressures: Diffraction and DFT

Figure 6 shows the measured x-ray-diffraction pattern of $LaAuSb_2$ at several pressures between 0–8.86 GPa from the second run using 4:1 methanol-ethanol pressure-transmitting medium. The pattern is similar at all pressures except for shift towards higher 2θ values with increasing pressure and thus reveals that there are no symmetry changing structural phase transitions in this pressure range. Data from the silicone oil run are given in Fig. S2, confirming again the absence of any symmetry changing structural phase transition. As reported in the section above, pressure decreases the CDW transition monotonically and it is fully suppressed at 3.6 GPa. To understand whether the structural properties play a role in suppressing the CDW transition, we have carefully investigated the lattice parameters as a function of pressure by Rietveld refinement analysis of the obtained diffraction data. Examples of the Rietveld refinement in both runs are given in Fig. S3. Both the lattice parameters show a rather continuous decrease. A careful look shows that there is a clear change in the trend above and below 3.8 GPa (see Fig. 7). The pressure run with PTM as silicone oil also indicated anomalies in the lattice parameters (see Fig. S4). In that case, the lattice parameter a is found to show a slope change from negative to positive above 3.5 GPa. In that case, there was also a change in trend that was noticeable in the out of plane lattice parameter around similar pressure (see Fig. S4). Varying hydrostatic conditions from 4:1 methanol-ethanol to silicone oil is not supposed to significantly modify the pressure dependence of the structural parameters [46]; however, in the case of $LaAuSb_2$, the effects that we observe are much marked. In this context, we recall

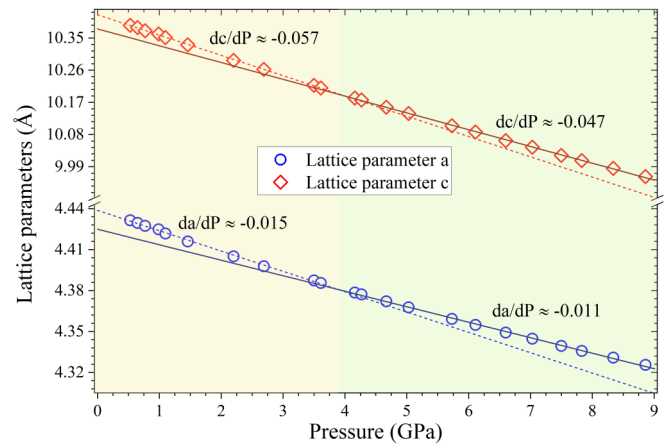

FIG. 7. Pressure dependence of lattice parameters. Solid and dotted lines in the panels correspond to a linear fit of the data in the pressure below and above 3.8 GPa regimes. Corresponding slopes are indicated in the graph.

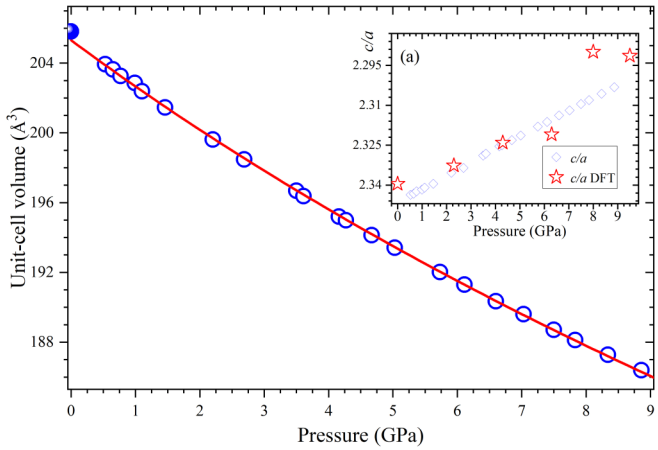

FIG. 8. Pressure dependence of unit-cell volume. Open circles are data from the high-pressure run. Filled circle at 0 GPa is from the temperature-dependent study. Solid red line is the result of a second-order Birch-Murnaghan equation of state fit to the data. Inset (a) shows the out of plane to in plane lattice parameter ratio from experiments (symbol diamond) and DFT (symbol star).

again the significant difference seen in the CDW properties of this system reported by different groups [25,35].

In Fig. 8 we present the volume vs pressure curve, which is found to vary smoothly without any strong anomalies. A second-order Birch-Murnaghan equation of state (EoS) can describe well the variation in the unit-cell volume in the studied pressure range. EoS fit provided the bulk modulus K to be 75.1 GPa, with zero-pressure unit-cell volume 205.31 Å^3 and pressure derivative of $K = 4$ (fixed). The calculated bulk modulus from DFT is 74 GPa, indicating a good match between experimental and DFT results.

Earlier studies have indicated that the pressure effect on c/a changes are clear indications of pressure-induced electronic topological transitions [47,48]. In $LaAuSb_2$ system, the suppression of the CDW may led to Fermi-surface topological changes, which under suitable conditions can even lead to Cooper pair formation which with a lowering of the temperature can acquire necessary coherence to lead to superconductivity. In fact, a recent study by Du *et al.* on a very similar system has reported a significant enhancement in the superconducting transition temperature upon the full suppression of the CDW [35]. Our resistivity measurements are limited to 4 K, thus nonpermitting the verification of possible superconducting states at very low temperatures upon the complete suppression of the CDW order. In Fig. 8 inset, we compare the experimental and DFT c/a ratio. DFT results show an anomaly in the c/a ratio above 7 GPa. Though the experimental data show a rather smooth change, lattice parameters showed a change in their linear trend above and below 3.8 GPa. We remark that the effect is much marked in the silicone oil run (see Fig. S4.) This is mostly due to the less hydrostatic nature in that run. But, we would also like to point out another possibility: the structural evolution of $LaAuSb_2$ may be extremely sensitive to the slightly varying hydrostatic conditions. To further probe this aspect, we have also undertaken DFT studies by varying the Au content. The decreasing Au content is found to result in a reduction of the

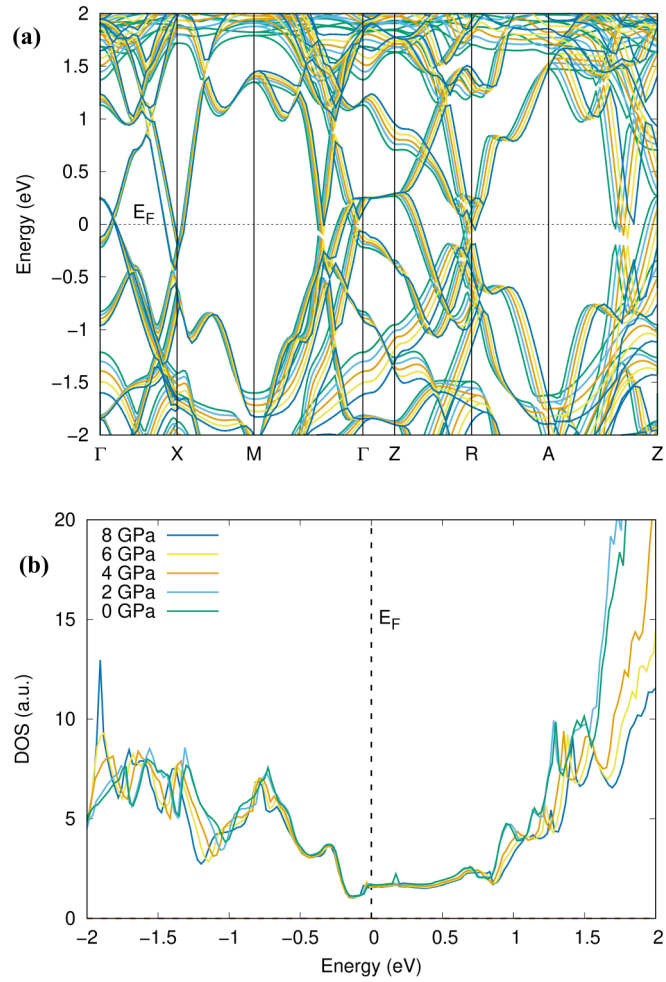

FIG. 9. Calculated electronic structure (a) and total density of states close to Fermi level (b) of $LaAuSb_2$ with GGA and PW91 functional as a function of energy under various pressures up to 8 GPa.

unit-cell volume (Fig. S5). Theoretical investigation showed the minimum unit-cell volume to be 211.054 Å^3 for the stoichiometric compound (see Fig. S6 and Table I).

To understand more about the possibility of the electronic topological transition, we carefully studied the electronic structure of $LaAuSb_2$ under various pressures. DFT study shows that in the pressure range 0–8 GPa, there is no significant change in the total DOS very close to Fermi level E_F [$\pm$ 0.3 eV in Fig. 9(b)]. However, there are changes in the total DOS with pressure due to increasing orbital overlaps. Results in the extended energy range for calculated electronic structure and total density of states up to 8 GPa are given in Fig. S7. A careful look at Fig. 9(b) reveals the changes in the total DOS are not following a continuous change (see also Fig. S7). In particular, changes are seen to occur above 6 GPa (for example, see changes around 0.7–1.4 eV). A closer look at the band structure [Fig. 9(a)] reveals interesting changes (see, for example, changes close to E, close to Γ point and bands crossing E_F in the A-Z direction). The positive phonon frequencies are obtained for the structure in this pressure range. Phonon frequencies at various pressures

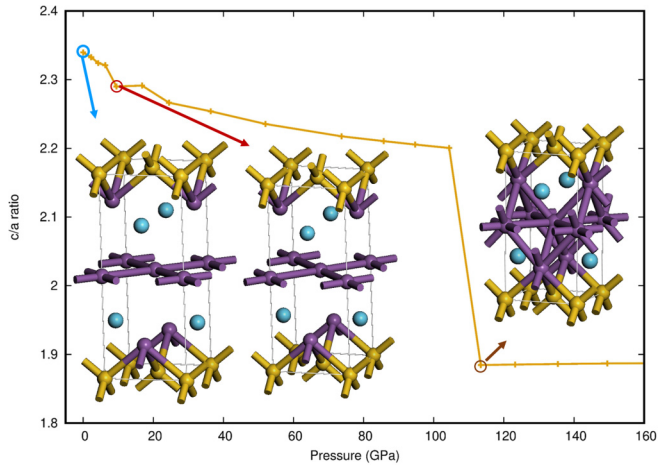

FIG. 10. Calculated c/a ratio as a function of pressure up to 150 GPa obtained from optimized unit cell.

in 0–8 GPa are shown in Fig. S8. A comparison of the ambient pressure and 8 GPa is provided in Fig. S9. These data underline the stability of the $LaAuSb_2$ to compression in this range.

D. Structural stability of $LaAuSb_2$: DFT

We now discuss the stability of the crystal structure to very high pressures up to 150 GPa from the DFT point of view. The calculated c/a ratio as a function of pressure clearly shows that the application of pressure significantly changed the cell ratio (Fig. 10). However, the symmetry analysis on the fully optimized structure clearly shows that the structure is still $P4/nmm$ even at 150 GPa where the c/a ratio is drastically changed. Calculated phonon spectra are positive also at 150 GPa (Fig. S10) indicating the stability of the structure. Site-projected phonon density of states for $LaAuSb_2$ at 150 GPa is presented in Fig. S11. The spectacular volume collapse that we observe in this system at high pressure above 110 GPa (see Fig. 10 and Fig. S12) merits further comments. As noted in the Introduction, $LaAuSb_2$ ternary antimonides share several structural similarities with layered iron pnictides. The interplay of several degrees of freedom in iron-based superconductors is a subject of intense research even recently [49–52]. In a seminal study, Kreyssig *et al.* showed a pressure-induced volume collapse in the tetragonal phase of $CaFe_2As_2$ [49], a 122 iron pnictide. The volume collapse that we see in the tetragonal phase of $LaAuSb_2$ seems to be of similar nature to the 122 iron-pnictide systems [49,50]; however, the critical pressure where this phenomenon occurs is much different in the two systems. DFT also seems to show a volume collapse at lower pressures around 10 GPa (see Fig. S14). A volume collapse without a symmetry change is envisaged to bring an electronic transition in terms of the valency, as shown for CeP under pressure [53]. However, as shown in the inset of Fig. 10, from DFT, we may expect the two types of Sb atoms to be in communication only above 100 GPa. Interestingly, temperature dependence of $LaAuSb_2$ shows a negative thermal expansion for the out of plane axis [Fig. 4(b)]. Such a phenomenon is also observed in several of the 122 iron pnictides [52]. These similarities call for a more careful comparative study of the 122 pnictides and ternary antimonides. It is often believed that the d electrons play an important role in the superconducting behavior of intermetallic compounds. So, the experimental search for new superconductors has been focused to a large extent on transition-metal compounds. The background for this is that transition-metal compounds usually possess a large DOS at the E_F, one of the ingredients required for high T_c than the main-group metal (sp) compounds. The BCS superconductors usually possess larger DOS at the E_F and the high T_c in conventional superconductors is related to the large $N(E_F)$ values as well as the strong coupling of selected phonon modes to the electronic system. From the above point of view, the presence of superconductivity in these type of materials from a conventional BCS mechanism is rather questionable. However, the fact that the ternary antimonides show several phenomena similar to the new class of iron-based 122 superconductors [49,50,52] demands the search for an unconventional mechanism behind the observed pressure-induced superconductivity.

IV. CONCLUSIONS

We have presented the results from a systematic synchrotron x-ray powder-diffraction study for $LaAuSb_2$ as a function of temperature (390 to 110 K) and pressure (up to 9 GPa). At ambient pressure, a CDW transition is observed ~83 K in this system due to the formation of Fermi nesting. X-ray diffraction at ambient pressure reveals that in plane and out of plane axes show opposite behavior with decreasing temperature, in particular, out of plane c axis develops a distinct change at ~250 K, much above the observed CDW transition at 83 K. The structural modulation occurring at 250 K may be a precursor effect to the CDW transition in this system. With increasing pressure, we found a decrease in the CDW transition temperature with complete suppression of the same about 3.6 GPa, where CDW transition temperature vs pressure relation is found to be linear. DFT indicates an anomaly in the pressure dependence of the out of plane to in plane lattice parameter ratio (c/a) within the pressure range 10 GPa. The calculated electronic structure indicated minor changes in the band structure in this pressure range. DFT analysis further indicates that the $P4/nmm$ structure is stable up to 150 GPa. The volume gets collapsed and c/a ratio is drastically changed above 100 GPa. Present results together with the earlier works on similar systems [26,35] shed light on the intriguing CDW transition and its relevance to other collective excitations in $LaAuSb_2$ ternary antimonides.

ACKNOWLEDGMENTS

The authors thank DST, Govt. India for support in executing the high-pressure diffraction experiments at Xpress beamline of the Elettra Sincrotrone Trieste (Proposal No. 20200321) and M. Polentarutti for in-house beamtime allocation at XRD1. S.A. wishes to thank DST (ASEAN, PURSE, FIST, JSPS, MES, and SERB), UGC-DAE CSR (Indore), MHRD-RUS (R&1), TANSCHE (Chennai), and BRNS (Mumbai) for the financial support. P.V. gratefully

acknowledge the Research Council of Norway for providing the computer time (under Projects No. NN2875k and No. NS2875k) at the Norwegian supercomputer facility. P.R. acknowledges the receipt of a fellowship from the ICTP Programme for Training and Research in Italian Laboratories, Trieste, Italy.

[1] H. K. D. H. Bhadeshia, and C. M. Wayman, 9-Phase transformations: Nondiffusive, in *Physical Metallurgy*, 5th ed., edited by D. E. Laughlin, and K. Hono (Elsevier, Amsterdam, 2014), p. 1021.

[2] R. E. Peierls, *Quantum Theory of Solids* (Oxford University Press, Oxford, 1955).

[3] G. Grüner, *Density Waves in Solids* (Addison-Wesley, Reading, MA, 1994).

[4] J. A. Wilson, F. J. Di Salvo, and S. Mahajan, Charge-density waves and superlattices in the metallic layered transition metal dichalcogenides, Adv. Phys. **24**, 117 (1975).

[5] X. Zhu, Y. Cao, J. Zhang, E. W. Plummer, and J. Guo, Classification of charge density waves based on their nature, Proc. Natl. Acad. Sci. **112**, 2367 (2015).

[6] G. Grüner, The dynamics of charge-density waves, Rev. Mod. Phys. **60**, 1129 (1988).

[7] S. V. Borisenko, A. A. Kordyuk, A. N. Yaresko, V. B. Zabolotnyy, D. S. Inosov, R. Schuster, B. Büchner, R. Weber, R. Follath, L. Patthey, and H. Berger, Pseudogap and Charge Density Waves in Two Dimensions, Phys. Rev. Lett. **100**, 196402 (2008).

[8] D. W. Shen, B. P. Xie, J. F. Zhao, L. X. Yang, L. Fang, J. Shi, R. H. He, D. H. Lu, H. H. Wen, and D. L. Feng, Novel Mechanism of a Charge Density Wave in a Transition Metal Dichalcogenide, Phys. Rev. Lett. **99**, 216404 (2007).

[9] K. Rossnagel, E. Rotenberg, H. Koh, N. V. Smith, and L. Kipp, Fermi surface, charge-density-wave gap, and kinks in $2H$-$TaSe_2$, Phys. Rev. B **72**, 121103(R) (2005).

[10] T. Straub, T. Finteis, R. Claessen, P. Steiner, S. Hüfner, P. Blaha, C. S. Oglesby, and E. Bucher, Charge-Density-Wave Mechanism in $2H-NbSe_2$: Photoemission Results, Phys. Rev. Lett. **82**, 4504 (1999).

[11] K. Zhang, X. Liu, H. Zhang, K. Deng, M. Yan, W. Yao, M. Zheng, E. F. Schwier, K. Shimada, J. D. Denlinger, and Y. Wu, Evidence for a Quasi-One-Dimensional Charge Density Wave in CuTe by Angle-Resolved Photoemission Spectroscopy, Phys. Rev. Lett. **121**, 206402 (2018).

[12] R. Gupta, A. Thamizhavel, P. Rodière, S. Nandi, K. P. Rajeev, and Z. Hossain, Electrical resistivity under pressure and thermal expansion of $LaPt_2Si_2$ single crystal, J. Appl. Phys. **125**, 143902 (2019).

[13] K. Machida, T. Kōyama, and T. Matsubara, Theory of charge-density-wave superconductors, Phys. Rev. B **23**, 99 (1981).

[14] A. M. Gabovich, A. I. Voitenko, J. F. Annett, and M. Ausloos, Charge-and spin-density-wave superconductors, Supercond. Sci. Technol. **14**, R1 (2001).

[15] B. Wang, Y. Liu, X. Luo, K. Ishigaki, K. Matsubayashi, W. Lu, Y. Sun, J. Cheng, and Y. Uwatoko, Universal phase diagram of superconductivity and charge density wave versus high hydrostatic pressure in pure and Se-doped $1T$-TaS_2, Phys. Rev. B **97**, 220504(R) (2018).

[16] G. Bilbro, and W. L. McMillan, Theoretical model of superconductivity and the martensitic transformation in A15 compounds, Phys. Rev. B **14**, 1887 (1976).

[17] C. A. Balseiro, and L. M. Falicov, Superconductivity and charge-density waves, Phys. Rev. B **20**, 4457 (1979).

[18] W. Lubczynski, S. V. Demishev, J. Singleton, J. M. Caulfield, L. D. de Jongh, C. J. Kepert, S. J. Blundell, W. Hayes, M. Kurmoo, and P. Day, A study of the magnetoresistance of the charge-transfer salt at hydrostatic pressures of up to 20 kbar: Evidence for a charge-density-wave ground state and the observation of pressure-induced superconductivity, J. Phys.: Condens. Matter **8**, 6005 (1996).

[19] J. J. Hamlin, D. A. Zocco, T. A. Sayles, M. B. Maple, J. H. Chu, and I. R. Fisher, Pressure-Induced Superconducting Phase in the Charge-Density-Wave Compound Terbium Tritelluride, Phys. Rev. Lett. **102**, 177002 (2009).

[20] X. Yang, Y. Zhou, M. Wang, H. Bai, X. Chen, C. An, Y. Zhou, Q. Chen, Y. Li, Z. Wang, J. Chen *et al.*, Pressure induced superconductivity bordering a charge-density-wave state in $NbTe_4$ with strong spin-orbit coupling, Sci. Rep. **8**, 6298 (2018).

[21] E. Morosan, H. W. Zandbergen, B. S. Dennis, J. W. G. Bos, Y. Onose, T. Klimczuk, A. P. Ramirez, N. P. Ong, and R. J. Cava, Superconductivity in Cu_xTiSe_2, Nat. Phys. **2**, 544 (2006).

[22] X. Zhu, W. Ning, L. Li, L. Ling, R. Zhang, J. Zhang, K. Wang, Y. Liu, L. Pi, Y. Ma, and H. Du, Superconductivity and charge density wave in $ZrTe_{3-x}Se_x$, Sci. Rep. **6**, 26974 (2016).

[23] S. Masubuchi, Y. Ishii, K. Ouija, T. Fukuhara, F. Shimizu, and H. Sato, Chemical substitution effect on CDW state in $LaAgSb_2$, JPS Conf. Proc. **3**, 011053 (2014).

[24] M. S. Triracial, S. L. Bud'ko, S. A. Law, M. E. Tillman, E. D. Mun, and P. C. Canfield, Hydrostatic pressure study of pure and doped $La_{1-x}R_xAgSb_2$ (R = Ce, Nd) charge-density-wave compounds, Phys. Rev. B **76**, 235110 (2007).

[25] C. N. Kuo, D. Shen, B. S. Li, N. N. Quyen, W. Y. Tzeng, C. W. Luo, L. M. Wang, Y. K. Kuo, and C. S. Lue, Characterization of the charge density wave transition and observation of the amplitude mode in $LaAuSb_2$, Phys. Rev. B **99**, 235121 (2019).

[26] L. Xiang, D. H. Ryan, W. E. Straszheim, P. C. Canfield, and S. L. Bud'ko, Tuning of charge density wave transitions in $LaAu_xSb_2$ by pressure and Au stoichiometry, Phys. Rev. B **102**, 125110 (2020).

[27] P. Wollesen, W. Jeitschko, M. Brylak, and L. Dietrich, Ternary antimonides $LnM_{1-x}Sb_2$ with Ln = La − Nd, Sm, Gd, Tb and M = Mn, Co, Au, Zn, Cd, J. Alloys Compd. **245**, L5 (1996).

[28] I. Hase, and T. Yanagisawa, Electronic band calculation of $LaTSb_2$ (T = Cu, Ag, Au), Phys. Proc. **58**, 42 (2014).

[29] K. D. Myers, S. L. Bud'ko, I. R. Fisher, Z. Islam, H. Kleinke, A. H. Lacerda, and P. C. Canfield, Systematic study of anisotropic transport and magnetic properties of $RAgSb_2$ (R = Y, La–Nd, Sm, Gd–Tm), J. Magn. Magn. Mater. **205**, 27 (1999).

[30] Y. Kamihara, T. Watanabe, M. Hirano, and H. Hosono, Iron-based layered superconductor La[$O_{1-x}F_x$]FeAs ($x = 0.05-0.12$) with $T_c = 26$ K, J. Am. Chem. Soc. **130**, 3296 (2008).

[31] Y. Muro, N. Takeda, and M. Ishikawa, Magnetic and transport properties of dense Kondo systems, $CeTSb_2$ (T = Ni, Cu, Pd and Ag), J. Alloys Compd. **257**, 23 (1997).

[32] L. Balicas, S. Nakatsuji, H. Lee, P. Schlottmann, T. P. Murphy, and Z. Fisk, Magnetic field-induced quantum critical point in $CeAuSb_2$, in *Low Temperature Physics: 24th International Conference on Low Temperature Physics - LT24*, edited by Y. Takano, S. P. Hershfield, S. O. Hill, P. J. Hirschfeld, and A. M. Goldman, AIP Conf. Proc. No. 850 (AIP, New York, 2006), p. 693.

[33] Y. Inada, A. Thamizhavel, H. Yamagami, T. Takeuchi, Y. Sawai, S. Ikeda, H. Shishido, T. Okubo, M. Yamada, K. Sugiyama, and N. Nakamura, An unusual hollow cylindrical Fermi surface of a quasi-two-dimensional compound $CeAgSb_2$, Philos. Mag. B **82**, 1867 (2002).

[34] C. Song, J. Park, J. Koo, K. B. Lee, J. Y. Rhee, S. L. Bud'ko, P. C. Canfield, B. N. Harmon, and A. I. Goldman, Charge-density-wave orderings in $LaAgSb_2$: An x-ray scattering study, Phys. Rev. B **68**, 035113 (2003).

[35] F. Du, H. Su, S. S. Luo, B. Shen, Z. Y. Nie, L. C. Yin, Y. Chen, R. Li, M. Smidman, and H. Q. Yuan, Interplay between charge density wave order and superconductivity in $LaAuSb_2$ under pressure, Phys. Rev. B **102**, 144510 (2020).

[36] See Supplemental Material at http://link.aps.org/supplemental/10.1103/PhysRevB.103.195126 for several additional information on the $LaAuSb_2$ system. These are: Ewald sphere reconstruction from single crystal diffraction and EDX spectrum (FIG S1); XRD pattern at different pressures from silicone oil run (FIG. S2); Rietveld refinement results (Fig. S3); Pressure dependent structural parameters from silicone oil run (Fig. S4); Calculated unit-cell volume vs Au defect concentration (Fig. S5); Theoretical energy-volume curve (Fig. S6); Calculated electronic DOS (Fig. S7 & Fig. S11); Calculated phonon spectra (Fig. S8, Fig. S9 & Fig. S10); and unit-cell volume from DFT till 150 GPa (Fig. S12).

[37] B. Joseph, N. Demitri, P. Lotti, A. Lausi, and P. Dore, Unraveling the peculiarities in the temperature-dependent structural evolution of black phosphorus, Condensed Matter **2**, 11 (2017).

[38] G. K. Selvan, D. Bhoi, S. Arumugam, A. Midya, and P. Mandal, Effect of pressure on the magnetic and superconducting transitions of $GdFe_{1-x}Co_xAsO$ ($x = 0, 0.1, 1$) compounds, Supercond. Sci. Technol. **28**, 015009 (2014).

[39] P. Lotti, S. Milani, M. Merlini, B. Joseph, F. Alabarse, and A. Lausi, Single-crystal diffraction at the high-pressure Indo-Italian beamline Xpress at Elettra, Trieste, J. Synchrotron Radiat. **27**, 222 (2020).

[40] G. Kresse, and J. Furthmüller, Efficient iterative schemes for ab initio total-energy calculations using a plane-wave basis set, Phys. Rev. B **54**, 11169 (1996).

[41] G. Kresse, and J. Furthmüller, Efficiency of ab-initio total energy calculations for metals and semiconductors using a plane-wave basis set, Comput. Mater. Sci. **6**, 15 (1996).

[42] J. P. Perdew, K. Burke, and M. Ernzerhof, Generalized Gradient Approximation Made Simple, Phys. Rev. Lett. **77**, 3865 (1996).

[43] A. Togo, F. Oba, and I. Tanaka, First-principles calculations of the ferroelastic transition between rutile-type and $CaCl_2$-type SiO_2 at high pressures, Phys. Rev. B **78**, 134106 (2008).

[44] H. J. Monkhorst, and J. D. Pack, Special points for Brillouin-zone integrations, Phys. Rev. B **13**, 5188 (1976).

[45] P. Vinet, J. H. Rose, J. Ferrante, and J. R. Smith, Universal features of the equation of state of solids, J. Phys.: Condens. Matter **1**, 1941 (1989).

[46] S. B. Pillai, B. Joseph, D. Upadhyay, C. Marini, and P. K. Jha, Pressure induced hydrogen order-disorder transition in β-$Ni(OH)_2$, J. Phys. Chem. C **125**, 2785 (2021).

[47] V. Rajaji, U. Dutta, P. C. Sreeparvathy, S. C. Sarma, Y. A. Sorb, B. Joseph, S. Sahoo, S. C. Peter, V. Kanchana, and C. Narayana, First-principles Structural, vibrational, and electrical properties of 1T-$TiTe_2$ under hydrostatic pressure: Experiments and theory, Phys. Rev. B **97**, 085107 (2018).

[48] A. Polian, M. Gauthier, S. M. Souza, D. M. Trichês, J. C. de Lima, and T. A. Grandi, Two-dimensional pressure-induced electronic topological transition in Bi_2Te_3, Phys. Rev. B **83**, 113106 (2011).

[49] A. Kreyssig, M. A. Green, Y. Lee, G. D. Samolyuk, P. Zajdel, J. W. Lynn, S. L. Bud'ko, M. S. Torikachvili, N. Ni, S. Nandi *et al.*, Pressure-induced volume-collapsed tetragonal phase of $CaFe_2As_2$ as seen via neutron scattering, Phys. Rev. B **78**, 184517 (2008).

[50] A. Ptok, M. Sternik, K. J. Kapcia, and P. Piekarz, Structural, electronic, and dynamical properties of the tetragonal and collapsed tetragonal phases of KFe_2As_2 as seen via neutron scattering, Phys. Rev. B **99**, 134103 (2019).

[51] A. Iadecola, S. Agrestini, M. Filippi, L. Simonelli, M. Fratini, B. Joseph, D. Mahajan, and N. L. Saini, Local structure of ReFeAsO (Re = La, Pr, Nd, Sm) oxypnictides studied by Fe K-edge EXAFS, Europhys. Lett. **87**, 26005 (2009).

[52] A. Rebello, J. J. Neumeier, Z. Gao, Y. Qi, and Y. Ma, Giant negative thermal expansion in La-doped $CaFe_2As_2$, Phys. Rev. B **86**, 104303 (2012).

[53] B. Joseph, R. Torchio, C. Benndorf, T. Irifune, T. Shinmei, R. Pottgen, and A. Zerr, Experimental evidence of an electronic transition in CeP under pressure using Ce L_3 XAS, Phys. Chem. Chem. Phys. **19**, 17526 (2017).